

Orbital Order Effect of Two-Dimensional Spin Gap System for CaV_4O_9

Nobuyuki KATOH * and Masatoshi IMADA **

Institute for Solid State Physics, University of Tokyo, 7-22-1, Roppongi, Minato-ku, Tokyo 106

(Received December 2, 2024)

Effects of possible orbital order in magnetic properties of two-dimensional spin gap system for CaV_4O_9 are investigated theoretically. After analyzing experimental data, we show that single orbital models assumed in the literature are insufficient to reproduce the data. To understand the origin of the discrepancy, we assume that in d^1 state of V, d_{xz} and d_{yz} orbitals have substantial contributions in the lowest-energy atomic level which leads to a double-degeneracy. We study possible configurations of the orbital order. By exact diagonalization and perturbation expansion, we calculate the susceptibility, wavenumber dependence of low-lying excitations and equal-time spin-spin correlations which is related to integrated intensity of the neutron inelastic scattering. These quantities sensitively depend on the configuration of the orbital order. The calculated results for some configurations of the orbital order reproduce many experimental results much better than the previous single-orbital models. However some discrepancy still remains to completely reproduce all of the reported experimental results. To understand the origin of these discrepancies, we point out the possible importance of the partially occupied d_{xy} orbital in addition to orbital order of partially filled d_{xz} and d_{yz} orbitals.

KEYWORDS: CaV_4O_9 , spin gap, orbital order

§1. Introduction

Since the spin gap was discovered in a typical two-dimensional material CaV_4O_9 ,¹⁾ the mechanism of the spin gap formation in this system has been intensively studied by many theoretical methods. 2, 3, 4, 5, 6, 7, 8, 9, 10, 11)

This material consists of VO_5 pyramid layers. Crystal structure of the VO_5 pyramid layer is shown in Fig.1(a). The oxygens constitute a complete square lattice while in the square lattice of the vanadium atoms, 1/5 of them are depleted. The vanadium atom is nearly located at the center of the pyramid constructed from four oxygens in the layer and one apical oxygen. Each VO_5 pyramid is connected by edge sharing. The unit cell of the layer includes two edge-shared

* Present address: National Research Institute for Metals, 1-2-1, Sengen, Tsukuba 305, Ibaraki

** Submitted to J.Phys.Soc.Jpn.

plaquettes of V atoms shown in Fig.1(a), because the apical oxygen of one edge-shared plaquette is located above the VO_2 plane while that of the other one is below the plane.

Fig. 1. (a) Crystal structure of VO_5 pyramid layer. Full circles represent vanadium atoms, while open circles are oxygen atoms. Apical oxygens are omitted in this figure. Shaded square area represents the unit cell of this system. Vectors \mathbf{a}_1 and \mathbf{b}_1 are the unit lattice vectors ; $\mathbf{a}_1 = 3\mathbf{x} - \mathbf{y}$ and $\mathbf{b}_1 = \mathbf{x} + 3\mathbf{y}$, respectively. Here \mathbf{x} and \mathbf{y} represent the unit lattice vectors of the square lattice composed of oxygens defined as $\mathbf{x} = a\mathbf{e}_x$ and $\mathbf{y} = a\mathbf{e}_y$. Parameter a is a lattice constant while \mathbf{e}_x and \mathbf{e}_y are unit vectors. (b) Four kinds of the superexchange couplings. Bold-gray, bold-black, thin-gray and thin-black lines represent the spin exchange couplings, J_{ep} , J_{ed} , J_{cp} and J_{cd} , respectively.

Since the valence of V atom is 4+, the d electron on V atom can be treated as a nearly localized spin with $S = 1/2$. In the literature, it has been assumed that a non-degenerate orbital on V atom is occupied.^{2,3,4,5,6,7,8,9,10,11)} Based on this assumption, the $S = 1/2$ antiferromagnetic Heisenberg (AFH) model with the nearest-neighbor and the next-nearest-neighbor exchange couplings has been introduced. When the nearest-neighbor exchange couplings are only taken into account, the system is described by the AFH model on the square lattice of the plaquettes, where each plaquette consists of four V atoms almost centered in the edge-shared pyramid. (We call this lattice plaquette lattice.) On the other hand, when only the next-nearest-neighbor exchange couplings are considered, the system is described by two disconnected square lattice of the plaquettes, where each plaquette is twice as large as and 45° tilted from the plaquette element of the previous case. In this case each plaquette consists of four corner-shared pyramid. Here, four different kinds of spin exchange couplings are introduced, as is shown in Fig.1(b). The spin exchange couplings between V atoms in the edge-shared and the corner-shared plaquettes are represented by J_{ep} and J_{cp} , respectively. While the spin exchange couplings connecting the edge-shared and the corner-shared plaquettes are J_{ed} and J_{cd} , respectively. In the literature, the case where $J_{\text{ed}} \simeq J_{\text{ep}}$ is taken as J and $J_{\text{cd}} \simeq J_{\text{cp}}$ is J' , has been mainly studied theoretically since only two kinds of spin exchange couplings should be derived from the previous single-orbital assumptions. The effects of the Jahn-Teller distortion, tilting of the pyramids and the spin-orbit couplings may cause the differences between J_{ed} and J_{ep} or between J_{cd} and J_{cp} . The theoretical methods such as perturbation expansions,^{2,3,4)} exact diagonalization,⁵⁾ mean field approximations,^{7,8)} quantum Monte Carlo method,^{2,9)} high-temperature expansions^{4,5,6)} and the density matrix renormalization group method¹⁰⁾ have led to the result that this system has a spin gap in the region around $J_{\text{ep}} > J_{\text{ed}}$ without frustration ($J' = 0$) or in the region $J' \simeq 0.5J$. Here the spin gap is defined as the energy difference between the singlet ground state and the lowest triplet states. In the above

mentioned regions, the origin of the spin gap is ascribed to the edge-shared plaquette singlet. The energy dispersion of the triplet states has been calculated by the perturbation expansion from the edge-shared plaquette singlet.^{2, 3, 4)} The wavenumber of the lowest energy excitation is (π, π) in the absence of the frustration, which is also obtained by the variational Monte Carlo method.¹¹⁾ However, it shifts to incommensurate wavenumbers as the frustration due to J' becomes relatively large.

Recently, the neutron inelastic scattering study for single crystal of CaV_4O_9 has been performed.^{12, 13)} The experiments indicate that the predictions from the theoretical studies for the conventional model are inconsistent with the experimental results. First of all, the wavenumber of the lowest energy excitation given by the experiments is $(0, 0)$ in the magnetic first Brillouin zone, which is different from the theoretical results. Here, the magnetic first Brillouin zone in the wavenumber space is expanded by the vectors $\tilde{\mathbf{a}}_2 = \tilde{\mathbf{a}}_1 + \tilde{\mathbf{b}}_1$ and $\tilde{\mathbf{b}}_2 = -\tilde{\mathbf{a}}_1 + \tilde{\mathbf{b}}_1$, as shown in Fig.2. It is $\sqrt{2} \times \sqrt{2}$ times larger than the first Brillouin zone of the unit cell expanded by the reciprocal lattice vectors $\tilde{\mathbf{a}}_1 = \mathbf{a}_1/10a^2$ and $\tilde{\mathbf{b}}_1 = \mathbf{b}_1/10a^2$, where a is a distance between the nearest-neighbor V atoms. Secondly, if the spin exchange couplings between V atoms are determined so as to reproduce the dispersion of the lowest triplet excitations in the experimental results, a large difference is resulted between the couplings, i.e. $J_{\text{cd}} = 0.088J_{\text{cp}}$ and $J_{\text{ep}} = J_{\text{ed}} = 0.395J_{\text{cp}}$,¹³⁾ which is hard to understand within the conventional framework.

Fig. 2. Brillouin zone of two-dimensional VO_2 plane in CaV_4O_9 lattice. Square surrounded by broken lines is the first Brillouin zone of the lattice, while the square with bold-solid lines is the magnetic first Brillouin zone obtained by the experiment.¹³⁾ The wavenumber \mathbf{q} is represented by the vectors $\tilde{\mathbf{a}}_1$ and $\tilde{\mathbf{b}}_1$. While \mathbf{k} is described by $\tilde{\mathbf{a}}_2 = \tilde{\mathbf{a}}_1 + \tilde{\mathbf{b}}_1$ and $\tilde{\mathbf{b}}_2 = -\tilde{\mathbf{a}}_1 + \tilde{\mathbf{b}}_1$, respectively. Here, the lattice constant between the nearest-neighbor V atoms is a .

In order to understand the contradiction between the experimental results and the theoretical ones, we should reconsider the mechanism of the spin gap formation for CaV_4O_9 . In this paper, we study effects of orbital degeneracy and orbital order which has been neglected in the literature. The crystal field from the oxygen ions on the corners of the pyramid lifts the degeneracy of t_{2g} orbitals in the atomic level. However, two orbitals whose wavefunctions are expanded by d_{xz} and d_{yz} orbitals may still be degenerate even in this crystal field. Then the effective Hamiltonian sensitively depends on configuration of the occupied d orbitals through the mechanism of the superexchange interaction if the occupied orbitals have substantial contributions from the d_{xz} and d_{yz} orbitals. In Section 2, we introduce several possible effective spin Hamiltonians with the orbital order. It is found that strength of spin exchange couplings strongly depends on patterns of the orbital occupancy. This

may explain the appearance of large difference in the spin exchange couplings needed to reproduce experimental results. In Section 3, we estimate the strength of the spin exchange couplings from analyses of the temperature dependence of the uniform magnetic susceptibility. We use the exact diagonalization (ED) method. Although the system size tractable by the ED is limited, the cases we studied show rather small system size dependence due to the opening the spin gap which makes it possible to infer the thermodynamic limit. Then we calculate the energy dispersion of the triplet states and the wavenumber dependence of the equal-time spin-spin correlation which is related to the integrated intensity of the neutron inelastic scattering within the perturbation expansion (PE). The important elements to explain the experimental results are pointed out. The origin of the spin gap in each case of the orbital order is also discussed. In Section 4, we compare these theoretical results with the experimental ones and discuss the importance of the orbital order. Section 5 is devoted to summary.

§2. Effective Hamiltonians

For the purpose of understanding the problems mentioned in the previous section, we consider several models for the spin gap formation. The Hamiltonian is given by the AFH model written as

$$H = \sum_{\langle i,j \rangle} J_{ij} \mathbf{S}_i \cdot \mathbf{S}_j, \quad (2.1)$$

where \mathbf{S}_i represents the spin operator with $S = 1/2$ at i site and J_{ij} is the spin exchange coupling between the spins at i and j sites.

In this study, we assume that the orbitals giving the lowest energy in the atomic level due to the crystal field are doubly degenerate. In other words, the ground state wavefunction has substantial weight of the d_{xz} and d_{yz} orbitals and that the d electron occupies these orbitals at least partially. Below we refer to occupied orbitals simply as d_{xz} or d_{yz} orbitals in this paper. However, it does not necessarily mean that those consist of pure d_{xz} and d_{yz} orbitals. What we need to make the proposals in this paper relevant is the double-degeneracy of occupied orbitals with d_{xz} and d_{yz} component contained. Even small contribution of d_{xz} and d_{yz} orbitals may make the exchange coupling sensitively dependent on the occupied orbitals. Although the static Jahn-Teller distortion or tilting of the pyramid could lift the degeneracy of d_{xz} and d_{yz} orbitals, we do not consider this effect within this study, because such static distortions have not been observed so far. Therefore, we investigate effects of the orbital order for the d_{xz} and d_{yz} orbitals. As is mentioned later, the strength of the spin exchange couplings between V atoms depends on the configuration of the occupied d orbitals on V atoms.

We consider the spin exchange couplings between the nearest as well as between the next-nearest neighbor V atoms through the superexchange mechanism, as is shown in Fig.3. In the first case, the V-O-V bonds make approximately right angle. Then the superexchange coupling works relevantly through the p_z orbital of the oxygen when the d electron occupies d_{xz} orbital on V atom and

Fig. 3. Lattice structure of V-O-V and configuration of occupied orbital. Figures (a) and (b) show the cases with the right angle of V-O-V. Figure (a) shows the case that the occupied d orbitals on V atoms are different, while (b) is the case with the same occupied orbital. Figures (c) and (d) show the cases with the straight line of V-O-V. The configurations of the occupied d orbitals in Fig.(c) and (d) are the same as those in Fig.(a) and (b), respectively.

the other d electron is localized at d_{yz} orbital on the other V atom shown in Fig.3(a). However, the superexchange coupling may be relatively small when the both d electrons occupy the same orbitals on each V atom shown in Fig.3(b). The reason is that one of the transfer integrals between p_z orbital on oxygen and one of the d orbitals is relatively small due to the symmetry of the wavefunction of these orbitals. In the second case, the V-O-V bonds make approximately straight line. Then the superexchange coupling works effectively when the d electrons are localized at the same orbitals which extend to the oxygen as shown in Fig.3(d). While the superexchange coupling should be relatively small in the case shown in Fig.3(c). When the d electrons occupy the orbitals both of which do not extend to the oxygen located between the V atoms, the strength of the superexchange couplings should be also relatively small. Consequently, the anisotropy of the spin exchange couplings arises through this mechanism.

Here, we introduce five models with the possible patterns of the orbital order as shown in Figs.4. The orbital patterns in Figs.4(a) and (b) are the cases where the electrons occupy the d orbitals alternately within the edge-shared plaquettes but in a uniform way from plaquette to plaquette. The relevant spin exchange couplings in Fig.4(a) are the edge-shared plaquette bonds J_{ep} , while the ones in Fig.4(b) are J_{ep} and J_{cd} . Figure 4(c) shows the case where the plaquette unit in Fig.4(a) and (b) are placed alternately. Figure 4(d) shows the case where all the occupied orbitals have the same symmetry. Figure 4(e) shows the case where the occupied d orbitals are alternating in the x -direction while are uniform in the y -direction. From here, we take the strengths of the relatively small spin exchange couplings as the same values. In reality, these value are not necessarily the same because these small couplings appear due to some small distortion of the lattice from the perfect square lattice. Then to study difference between them, these small effects have to be considered. This point is discussed in detail in Section 4. In other possible patterns of the orbital order, the magnetic unit cell becomes more complicated. In this paper, we do not consider these more complicated possibilities.

§3. Results

In this section, we study magnetic properties for the models in Figs.4(a), (b) and (c) in more detail than for (d) and (e) since the configuration of the occupied orbitals in the edge-shared

Fig. 4. Five possible patterns of orbital order viewed in the projection to the xy plane. Bold lines connecting V atoms represent the dominant superexchange couplings. The symbols on V atoms represent the d_{xz} and d_{yz} orbitals schematically. (a) A case with the alternating pattern of the orbitals in the edge-shared plaquette. The filled orbitals are “tiled” in a uniform way among different plaquettes. (b) This is the same as the one in Fig.(a). However, the d_{xz} and d_{yz} orbitals are replaced each other. (c) The case where the orbital in all the nearest-neighbor V atoms are occupied always in the alternating configuration. (d) The case that all the orbitals are occupied uniformly. (e) The case that the occupied orbitals are alternating in the x -direction while are uniform in the y -direction.

plaquette for these models has four-fold rotational symmetry which appears to be consistent with experimental observations.¹³⁾

3.1 Uniform Magnetic Susceptibility

In this subsection, we determine the amplitude of the relevant spin exchange couplings and the other relatively small ones to reproduce the temperature dependence of the uniform magnetic susceptibility χ given by the experiments. Here, we assume that eq.(2.1) is an effective spin Hamiltonian of magnetic properties below 700K. We calculate the χ of 16-site system by the ED with the periodic boundary condition. The uniform magnetic susceptibility is defined as

$$\chi = \frac{\beta}{N} \frac{\text{Tr} \sum_i \sum_j S_i^z S_j^z \exp(-\beta \epsilon_n)}{\text{Tr} \exp(-\beta \epsilon_n)}, \quad (3.1)$$

where β represents the inverse temperature and N is the number of site. In terms of comparison with the experimental data in the unit of emu/g, we should multiply our data with energy scale J by a factor $4N_A g^2 \mu_B / J k_B M$ with N_A the Avogadro number, μ_B the Bohr magneton, k_B the Boltzmann constant and M the gram per mole. The factor 4 comes from the number of V atoms in a unit cell. The parameter J depends on each model. Here, the g -factor is taken as a fitting parameter. The experimental data show a peak at a temperature about $T_p \simeq 110\text{K}$. The temperature T^* where the amplitude of χ becomes a half of that at T_p is about 595K. We choose the amplitude of the spin exchange couplings so as to give the best fit between the ED and the experimental results in the region above T_p .

Figure 5(a) shows the temperature dependence of the χ for the model shown in Fig.4(a). The fitting of the data leads to the spin exchange coupling J_{ep} is 183K, while relatively small ones are $J_{ed} = J_{cp} = J_{cd} = 97\text{K}$, respectively. The ratio J_{ed}/J_{ep} is 0.53. The g -factor is 1.71, which is rather small compared to $g \simeq 2.0$. In principle, the mechanism which reduces the value of the g factor estimated from χ in experiments could exist. One possibility is an effect of small spin-orbit couplings. However, we do not discuss this point in this paper. As a reference, the data not only for 16-site system but also for 8-site system are shown in Fig.5(a). The size dependence appears below T_p . However, the finite size effect is small above T_p , which justifies the present estimate of

the spin exchange couplings to take as the value in the thermodynamic limit.

The spin gap for 8-site, 16-site and 24-site systems were calculated. The size dependence of the spin gap is shown in the inset in Fig.5(a). If we assume that the fitting function for two-dimensional spin gap system has a form as $\Delta_s(N) = \Delta_s(\infty) + \frac{A}{N}$, the spin gap extrapolated to the thermodynamic limit is estimated to be about 101K, namely $\Delta_s/J_{\text{ep}} = 0.550$. The reason for taking this fitting function is as follows. The energy dispersion of the triplet excitation near the wavenumber with the lowest energy excitation is approximated as $\epsilon_T(\mathbf{k}) = \Delta_s + c_x k_x^2 + c_y k_y^2$ for sufficiently small k_x and k_y , where Δ_s represents the bulk spin gap. Using the periodic boundary conditions, the wavenumber $k_x(k_y)$ has a $L_x^{-1}(L_y^{-1})$ correction, where $L_x(L_y)$ is the number of sites in the $x(y)$ -direction. Because L_x and L_y are taken as $N^{-1/2}$ in two dimensions, the above fitting function is obtained. If the energy dispersion can be approximated by the quadratic form in a wide range of the wavenumber space, the fitting function reduced from the quadratic dispersion may be available even in small size systems. This model may belong to this case.

Fig. 5. Temperature dependence of uniform magnetic susceptibility for five models. Figures (a), (b), (c), (d) and (e) correspond to χ for the models in Figs.4 (a), (b), (c), (d) and (e), respectively. Bold-gray lines represent the experimental result. Insets show the extrapolation of the spin gap as a function of N in the ED results.

For the case shown in Fig.5(b), we take the relevant spin exchange couplings as $J_{\text{cd}} > J_{\text{ep}}$, for example, $J_{\text{ep}} = 0.9J_{\text{cd}}$. The reason is discussed in the next subsection. Figure 5(b) shows the temperature dependence of the χ . In a similar way, the relevant spin exchange couplings are estimated to be $J_{\text{cd}} \sim 185\text{K}$ and $J_{\text{ep}} \sim 166\text{K}$, while the relatively small ones are $J_{\text{cp}} = J_{\text{ed}} = 85\text{K}$. The ratio $J_{\text{cp}}/J_{\text{cd}}$ is 0.46. The g-factor is 1.72. In this case, one should be careful in estimating the spin gap from the data only for small size systems since the system seems to be near the critical point where the spin gap vanishes. Beyond the critical point when the spin gap disappears, the energy dispersion of the triplet states near the lowest excitation is expected to have a form as $\epsilon_T(\mathbf{k}) = \sqrt{c_x k_x^2 + c_y k_y^2}$, namely, a linear dispersion. As the system with the spin gap is close to the critical point, the wavenumber space where the form of the energy dispersion is approximated to be quadratic becomes narrower and narrower while the linearly dispersive region becomes wider. Then the leading term of the finite-size correction may crossover from $N^{-1/2}$ for small system size to N^{-1} for large system size. Here we take the form $\Delta_s(N) = \Delta_s(\infty) + \frac{A}{\sqrt{N}}$ as the fitting function. We have tried extrapolations by using two types of the fitting function. However, we found that the leading term of the finite size correction is $N^{-1/2}$ rather than N^{-1} in this case due to the limitation of the system size. Using this fitting function, the spin gap extrapolated to the thermodynamic limit is estimated to be about 34K, or $\Delta_s/J_{\text{cd}} = 0.186$. From the above reason, this estimate of

the spin gap is expected to give a slight underestimate. In this paper, in order to estimate the bulk spin gap, these two fitting functions are employed according as the situation.

In Fig.4 (c), the relevant spin exchange couplings are divided into two groups. One is the nearest-neighbor spin exchange coupling J and the other is the next-nearest-neighbor one J' . We consider the case that J' is larger than J and the other relatively small exchange couplings are neglected. The reason is discussed in the next subsection. Then the parameters J and J' are estimated to be 90K and 237K, respectively. The ratio J/J' is 0.38. The g -factor is 1.68. The relatively large spin gap survives in the thermodynamic limit and is estimated to be $\Delta_s/J' \simeq 0.564$ or 133K when we use the fitting function $\Delta_s(N) = \Delta_s(\infty) + \frac{A}{N}$.

The values of the spin gap for the first and the third model are close to the one in the experimental results. However, in the second case, the spin gap value is much smaller than the experimental one.

3.2 Origin of Spin Gap and Triplet Energy Dispersion

We consider the mechanism of the spin gap formation. To investigate the dispersion of triplet excitations, the perturbation method is useful since it is found by the analysis mentioned in the previous subsection that the strength of the relevant spin exchange couplings is relatively large compared to the others. In the case shown in Fig.4 (a), the term in eq.(2.1) including the relevant spin exchange coupling J_{ep} is treated as the unperturbed Hamiltonian, while the other terms are the perturbed ones. The strength of the other spin exchange couplings is taken as J . The singlet ground state of the isolated edge-shared plaquette is the resonating valence bond (RVB) singlet. Then the ground state of the unperturbed Hamiltonian is the product state of the RVB singlets on the edge-shared plaquettes. The origin of the spin gap is understood by the edge-shared plaquette singlet. The lowest excited state of the plaquette is the extended state of the triplet pair in the RVB state. Then the first excited states of the unperturbed Hamiltonian are constructed from the triplet state on one of the plaquettes and the singlets on the others. The degeneracy is lifted by the first-order perturbation through the transfer of the triplet due to the translational invariance, which yields the dispersion of the triplet states. We calculate the energy difference between the ground state and the triplet states within the second-order PE. The detailed procedure is explained in Appendix A. Figure 6 (a) shows the energy dispersion of the triplet excitation $\Delta_s(\mathbf{k})$. The wavenumber shown as (k_x, k_y) represents the vectors $k_x \tilde{\mathbf{a}}_2 + k_y \tilde{\mathbf{b}}_2$ with $\tilde{\mathbf{a}}_2 = \tilde{\mathbf{a}}_1 + \tilde{\mathbf{b}}_1$ and $\tilde{\mathbf{b}}_2 = -\tilde{\mathbf{a}}_1 + \tilde{\mathbf{b}}_1$. The first magnetic Brillouin zone is expanded by $\tilde{\mathbf{a}}_2$ and $\tilde{\mathbf{b}}_2$ as shown in Fig.2. In this case, the wavenumber of the lowest excitation is (0,0). Since a strong antiferromagnetic correlation due to J_{cp} is larger than the one due to J_{ed} in this model, the triplet states which have a strong in-phase correlation between the nearest-neighbor edge-shared plaquettes become the lowest excited states. The amplitude of the spin gap at (0,0) calculated by the second-order PE is $0.575J_{ed}$, which is close to the one estimated by the ED and is also consistent with the experimental result. These behaviors qualitatively reproduce the experimental results.

Fig. 6. Wavenumber dependence of triplet and singlet excited state energies for three models. Figures (a), (b) and (c) correspond to the models shown in Figs.4 (a), (b) and (c), respectively. Filled circles with error bar represent the experimental results.¹³⁾

In the case shown in Fig.4 (b), the terms with the relevant spin exchange couplings J_{ep} and J_{cd} are treated as the unperturbed Hamiltonians, while the other terms are the perturbed ones. In the $J_{\text{cd}} > J_{\text{ep}}$ case, the product state of the dimer pairs on J_{cd} bonds is the unperturbed ground state. Then the origin of the spin gap is ascribed to the corner-shared dimer singlets. The lowest excited states of the edge-shared plaquette are the product states of the triplet pair on one J_{cd} bond and the singlet pair on the other J_{cd} bonds. Because two kinds of triplet states exist, the lowest excited states are six-fold degenerate, which is also different from the previous case. We calculate the energy gap between the singlet state and those triplet states in a similar way. Figure 6 (b) shows the energy dispersion of the triplet states. The degeneracy is lifted by the first-order perturbation and the bonding and the anti-bonding triplet states appear. The wavenumbers of the lowest excitations are $(0, \pi)$ and $(\pi, 0)$. The spin gap is $0.197J_{\text{cd}}$, which is consistent with the value obtained by the ED. In this case, the square area surrounded by the lines connecting the nearest-neighbor points of the lowest excitation becomes a half of the original first magnetic Brillouin zone in the wavenumber space, which contradicts the experimental results.

In the model shown in Fig.4 (c), the ground state of the Hamiltonian given by the relevant spin exchange couplings is not straightforwardly obtained since the system has no isolated terms. To understand the mechanism of the spin gap formation, we neglect the small spin exchange couplings other than J and J' in this model. We consider three possible ground states and the origins of the spin gap for the Hamiltonian with only the relevant spin exchange couplings. To clarify three possibilities with the help of the perturbation method, the relevant terms are divided into two parts, unperturbed and perturbed terms. In the first case, the unperturbed Hamiltonian is taken as the term with J_{ep} while the others are the perturbed ones. Then the ground state of the unperturbed Hamiltonian is represented by the edge-shared plaquette singlet. In the second case, we take the unperturbed Hamiltonian as the J_{ed} term. Then the ground state is described by the edge-shared dimer singlet. In the third case, the unperturbed Hamiltonian is the term with the next-nearest-neighbor spin exchange couplings. Then the ground state is represented by the four-site stripe singlet. Since the first and the second cases have been already investigated,^{2, 3)} we concentrate on the third case. Then the amplitudes of the nearest and the next-nearest neighbor couplings are chosen as J and J' , respectively. Figure 7 shows the ground state energy per site

as a function of the strength of the spin exchange coupling $J/(J + J')$ calculated by the PE. The detailed calculation by the PE is written in Appendix B. The ground state described by the stripe

Fig. 7. Ground state energy per site $\epsilon_g/(J + J')$ as a function of $J/(J + J')$. Bold, broken and dash-dotted lines represent the ground state energy by the second-order perturbation from the plaquette singlet, dimer singlet and stripe singlet, respectively.

singlet is favored when $J/(J + J')$ is smaller than 0.483, or the ratio J/J' is smaller than 0.932. The system with $J = 90\text{K}$ and $J' = 237\text{K}$ estimated by the ED belongs to the stripe singlet phase as shown in Fig.7. Therefore, we may conclude that the stripe singlet is a possible mechanism of the spin gap formation in this model. We calculate the triplet dispersion as shown in Fig.6(c). The ground state is the product state of the stripe singlet for the unperturbed Hamiltonian. The magnetic unit cell in the real space contains two stripes crossing each other. Then the lowest triplet states in the unit cell are six-fold degenerate. Similarly to the analysis for the model given in Fig.4(b), the bonding and anti-bonding triplet states appear. The spin gap is $0.539J'$, which is close to the value obtained by the ED and is also close to the experimental result. However, the wavenumbers of the lowest excitations are $\pi\tilde{\mathbf{a}}_1$ and $\pi\tilde{\mathbf{b}}_1$ respectively, which is inconsistent with the experimental results. The magnetic periodicity is also different from the experimental one, since the magnetic first Brillouin zone is the same as that of the unit lattice. In this model, small exchange couplings in the corner-sharing have been neglected. They may change the quantitative feature such as band-width of the triplet dispersion. However, an effect due to them is very small since both of the occupied d orbitals on V atoms do not extend to the oxygen. Qualitative aspects such as the origin of the spin gap and the magnetic periodicity are not affected by these small exchange couplings.

3.3 Scattering Intensity

We investigate the scattering intensity of the neutron inelastic scattering given by the experiments. The scattering intensity is proportional to the Fourier component of the spin-spin correlation written as

$$I(\mathbf{q}, \omega) \propto \int dt e^{i\omega t} \langle \mathbf{S}(\mathbf{q}, t) \cdot \mathbf{S}(-\mathbf{q}, 0) \rangle, \quad (3.2)$$

where

$$\mathbf{S}(\mathbf{q}, t) = N^{-\frac{1}{2}} \sum_i \mathbf{S}_i(t) e^{-i\mathbf{q} \cdot \mathbf{r}_i}, \quad (3.3)$$

and $\langle \cdots \rangle$ represents the thermal average. The wavenumber \mathbf{q} are expanded by the vectors $\tilde{\mathbf{a}}_1$ and $\tilde{\mathbf{b}}_1$, namely we take q_x axis in the $\tilde{\mathbf{a}}_1$ direction and q_y in the $\tilde{\mathbf{b}}_1$ direction. When the temperature is sufficiently lower than the spin gap, eq.(3.2) is approximated by the transition probability from

the ground state $|\text{g.s.}\rangle$ to the triplet states $|n\rangle$, which is described as

$$I(\mathbf{q}, \omega) \propto \sum_n |\langle n | \mathbf{S}(\mathbf{q}) | \text{g.s.} \rangle|^2 \delta(\omega - E_n + E_g), \quad (3.4)$$

where the summation is restricted to the triplet states and E_n and E_g are the energy of the triplet states and the ground state, respectively. Here, when we calculate eq.(3.4), we use the wavefunctions of $|n\rangle$ and $|\text{g.s.}\rangle$ obtained by the PE, which is written in Appendix A in detail. The integrated intensity of the neutron inelastic scattering is obtained theoretically by integrating eq.(3.4) over ω , described as

$$I(\mathbf{q}) \equiv \int d\omega I(\mathbf{q}, \omega) \propto \sum_n |\langle n | \mathbf{S}(\mathbf{q}) | \text{g.s.} \rangle|^2. \quad (3.5)$$

Figures 8(a),(b) and (c) show the wavenumber dependence of the integrated intensity calculated by the PE. The experimental results are also shown in these figures. Especially, Figs.8(a) and (c) indicate important points. In the case shown in Fig.4(a), since the nearest-neighbor antiferromagnetic correlation due to J_{ep} is dominant, the scattering intensity has a minimum at $(\pi/a)\mathbf{e}_x$ and becomes larger as the wavenumber approaches $(\pi/a)\mathbf{e}_x + (\pi/a)\mathbf{e}_y$. While in the cases shown in Figs.4(b) and (c), since the next-nearest-neighbor antiferromagnetic correlation is dominant, the scattering intensity has a maximum at $(\pi/a)\mathbf{e}_x$ and becomes smaller as the wavenumber approaches $(\pi/a)\mathbf{e}_x + (\pi/a)\mathbf{e}_y$. From this result, experimental results indicate that the next-nearest-neighbor antiferromagnetic correlation is strong.¹³⁾ This supports the models in Figs.4(b) and (c). However, the wavenumber dependence for the model in Figs.4(c) is qualitatively different from the experimental results as shown in Figs.8(a) and (b). Therefore, the experimental results are rather consistent with the integrated intensity for the model shown in Fig.4(b) than those for the models shown in Figs.4(a) or (c).

Fig. 8. Wavenumber dependence of the integrated intensity for three models shown in Fig.4(a),(b) and (c). The wavenumber \mathbf{q} in Figures (a), (b) and (c) are represented by $\mathbf{q} = 2\pi(\tilde{\mathbf{a}}_1 + k\tilde{\mathbf{b}}_1)$ with $0.5 < k < 1.5$, $\mathbf{q} = 2\pi(h\tilde{\mathbf{a}}_1 + \tilde{\mathbf{b}}_1)$ with $1 < h < 2$ and $\mathbf{q} = 2\pi[(1 + \delta)\tilde{\mathbf{a}}_1 + (1 - \delta)\tilde{\mathbf{b}}_1]$ with $0 < \delta < 1$, respectively. Filled circles represent the experimental results given by Kodama *et al.*¹³⁾ The right ordinates represent the scale of the integrated intensity of the neutron inelastic scattering experiments. Here, the value 200 counts/5500kmon in the experiments corresponds to 0.04 obtained by the PE. This gives the best fit of the data for the model shown in Fig.4(b) with the experimental results.

§4. Discussion

To understand the mechanism of spin gap in CaV_4O_9 , we have studied the orbital-order dependence of the physical quantities such as the uniform magnetic susceptibility, the energy dispersion of the triplet states and the integrated scattering intensity. Before discussing these results, we show

the temperature dependence of χ for the system with $J_{\text{cp}} = 171\text{K}$, $J_{\text{cd}} = 15\text{K}$ and $J_{\text{ep}} = J_{\text{ed}} = 68\text{K}$. These parameter values are the ones suggested by an analysis of the neutron inelastic scattering experiments.¹³⁾ The uniform magnetic susceptibilities for 8-site and 16-site systems are calculated

Fig. 9. Temperature dependence of the uniform magnetic susceptibility for the model with $J_{\text{cp}} = 171\text{K}$, $J_{\text{cd}} = 15\text{K}$ and $J_{\text{ep}} = J_{\text{ed}} = 68\text{K}$. Broken and solid curves represent χ for 8-site and 16-site systems calculated by the ED, respectively, while the bold-gray line is the experimental result.

by the ED. The theoretical and the experimental results are shown in Fig.9. The size dependence is almost negligible and the numerical result of the χ for 16-site system may be regarded as the one in the thermodynamic limit. Since it is difficult to estimate the amplitude of the spin exchange couplings and the g -factor from the high temperature expansion, the g -factor is taken as 1.7 here, which is nearly the same as the value obtained by the analysis mentioned in the previous section. Figure 9 indicates that a qualitative difference between the experimental and theoretical results appears around the peak temperature. We may conclude that the parameters suggested by the analysis of the neutron inelastic scattering¹³⁾ are not consistent with the experimental result of the uniform magnetic susceptibility.

In Section 3, we have mainly studied the cases in Figs.4(a)-(c). Here, we briefly discuss the cases in Figs.4(d) and (e) for completeness. Figure 5(d) and (e) show the temperature dependences of χ . For the model in Fig.4(d), strength of the relevant spin exchange coupling J_{R} and the other small ones J are estimated to be 159K and 111K, respectively. The ratio J/J_{R} is 0.70. The g -factor is 1.71. The amplitude of the spin gap is extrapolated to be about 29K or $\Delta_{\text{s}}/J_{\text{R}} \simeq 0.179$. For the model in Fig.4(e), J_{R} and J are estimated to be 207K and 89K, respectively. The ratio J/J_{R} is 0.43. The g -factor is 1.70. The amplitude of the spin gap is about 3.6K or $\Delta_{\text{s}}/J_{\text{R}} \simeq 0.017$. In both cases, the model with given parameters J_{R} and J seems to be near the critical point because the leading term of the finite size correction in the fitting function is $N^{-1/2}$ rather than N^{-1} and the extrapolated values of the spin gap are very small. From the perturbational results, the origin of the spin gap for these models may also be described by the stripe singlet as well as the case in Fig.4(c).

Here, we discuss more quantitative aspects of the magnetic properties. We first discuss the temperature dependence of χ . The experimental results for the χ have not been well understood by the model with only the nearest-neighbor interaction, i.e. $J_{\text{cp}} = J_{\text{cd}} = 0$. In experiments, the spin gap Δ_{s} , the peak temperature T_{p} and the temperature T^* which gives a half amplitude of χ at T_{p} are 107K, 110K and 595K, respectively. The ratios $\Delta_{\text{s}}/T_{\text{p}}$ and T^*/T_{p} are 0.97 and 5.41, respectively. The peak temperature is relatively small compared to the spin gap and χ decays

rapidly below T_p . The numerical results for the model with the nearest-neighbor interactions have several different features from the experimental ones.^{2,9)} For example, the ratios Δ_s/T_p and T^*/T_p for the isolated plaquette model ($J_{ed} = 0$) are 1.28 and 3.83, respectively. In the plaquette singlet regions, these ratios become small as J_{ed} becomes large. While the ratios Δ_s/T_p and T^*/T_p for the isolated dimer model ($J_{ep} = 0$) are 1.60 and 3.48, respectively. In the dimer singlet regions, these ratios also become small as J_{ep} becomes large. Then the ratios estimated from the experiments are no longer reproduced from this model. We consider several possible reasons of this discrepancy from the experimental results below T_p . One is that the frustration due to the next-nearest-neighbor couplings reduces the band width of the triplet dispersion while keeps the strength of the spin gap, as has already been pointed out.³⁾ The other is that the low-lying excitations from the singlet ground state are not only the triplet states but also the singlet states. For example, in the case shown in Fig.4(b), the singlet dispersion exists in the low energy region, as shown in Fig.6(b). These singlet excited states are constructed from the product states of the lowest excited singlet state on one of the edge-shared plaquettes and the corner-shared dimer singlets on the others for the unperturbed Hamiltonian. Within the PE, the energy gap between the lowest singlet excitation and the ground state is comparable to the spin gap. In addition, since the singlet dispersion is nearly flat, the energies of the singlet excitations are lower than those of the triplet excitations in a wide region in the Brillouin zone. Then at the temperature around the singlet-singlet gap, χ decays rapidly since the strength of the denominator in eq.(3.1) increases relatively due to the increase of the weight of the excited singlet states. In order to discuss the possibility of the existence of the low-lying excitation of the singlet states, the detailed analysis of the experimental results for the specific heat is needed because the temperature dependence of χ below the spin gap temperature or the neutron inelastic scattering do not contain the information about the singlet excitations directly.

Next, we discuss the treatment of the spin exchange couplings. The spin exchange couplings have been divided into two groups. One is strong and the others are relatively small. The same value has been assigned for the values of the other relatively small couplings. This weaker bonds have minor contributions to physical properties and do not change the essential feature obtained in Sec.3. However, within these weaker bonds, it is possible that the amplitude of the nearest-neighbor couplings becomes twice as large as that of the next-nearest-neighbor couplings. Because the number of the path for the superexchange mechanism is two in the nearest-neighbor case while it is one in the next-nearest-neighbor one. If this estimate is adopted, for example in the case shown in Fig.4(a), the band width of the triplet dispersion becomes narrow and the wavenumber giving the lowest excitation shifts from $(0,0)$ to (π,π) within the second-order PE. Since, in the terminology of the perturbation method, the transfer energy of the triplet between the nearest-neighbor edge-shared plaquettes is determined by $J_{ed} - 2J_{cp}$ within the first-order PE, it vanishes

at $J_{\text{ed}} = 2J_{\text{cp}}$. The higher-order perturbation may change the wavenumber of the lowest excitation according as the sign of the transfer energy of the triplet or the amplitudes of the nearest and the next-nearest neighbor couplings.

Through this study, we have concentrated on the superexchange mechanism for the d_{xz} and the d_{yz} orbitals. In the real materials, however, there are several possible subtleties which further invalidate the assumption that the amplitude of the relatively small nearest-neighbor couplings is twice as large as that of the relatively small next-nearest ones. One is the contribution from the superexchange mechanism in the d_{xy} orbital since the wavefunction of the occupied orbital may also have a d_{xy} component in the real material. Due to this contribution, the next-nearest-neighbor couplings become antiferromagnetic and relevant. Another is the contribution from the direct exchange mechanism for both the d_{xy} orbital and the d_{xz} and d_{yz} orbitals. Since the bonding of the t_{2g} orbitals with the p_z orbital on oxygen is not σ bonding but π bonding, the effect of the direct exchange mechanism may be relatively strong compared to that of the superexchange mechanism. The detailed character of the direct exchange couplings may depend on the symmetry of the wavefunction and the distance between the V atoms. The contributions from tilting of the pyramid or the Jahn-Teller distortion may also influence the exchange coupling. Detailed quantitative analysis for the spin exchange couplings remain for further studies.

Finally, we discuss the importance of the d_{xz} and d_{yz} orbitals in the magnetic properties for CaV_4O_9 . In the real material, the wavefunction lying near the Fermi energy level may be the linear combination of the d orbitals. In this context, Marini and Khomskii¹⁶⁾ also pointed out the importance of the orbital order. They discussed the effect of the crystal field and estimated the coefficient of the linear combination of the d_{xz} and d_{yz} orbitals in the wavefunction. The given stable orbital is tilted and has a chirality. They concluded that the relevant spin exchange coupling is J_{ed} and the origin of the spin gap is an edge-shared dimer singlet. They proposed that the next strongest spin exchange couplings are the next-nearest-neighbor ones and J_{ep} is weakly ferromagnetic. In this case, however, the nearest-neighbor spin correlation is enhanced and the out-of-phase correlation between the nearest-neighbor edge-shared dimer singlets should be strong due to the next-nearest-neighbor antiferromagnetic spin exchange couplings and weakly ferromagnetic J_{ep} . These contradict the reported experimental results.¹³⁾

Neutron measurement suggests substantial antiferromagnetic correlations for the next-nearest-neighbor pair of V. This is naturally explained by the occupation of d_{xy} orbital. However, if only d_{xy} orbitals are occupied, it is hard to justify the model by Kodama *et al.*¹³⁾ where a much larger J_{cp} than J_{cd} is assumed. Aside from details it appears indeed necessary to take different J_{cp} and J_{cd} to reproduce the neutron data. Our model of orbital order can explain why the two next-nearest-neighbor spin exchange couplings differ. However, simple model with only d_{xz} and d_{yz} occupations appears to be insufficient to explain both of the susceptibility and neutron results

simultaneously as we discussed in this paper. All the above results imply, within this framework, that the wavefunction is in fact represented by a linear combination of the d_{xy} orbital and the other t_{2g} orbitals with the orbital order. We propose that the ground state is described as the wavefunction with large weight of d_{xy} orbital superposed with the ordered d_{xz} and d_{yz} orbitals given in Fig.4(a). In this case, the basic origin of the spin gap may be a corner-shared plaquette singlet. Then the next-nearest-neighbor antiferromagnetic spin correlation becomes relatively large since the large weight of d_{xy} orbital enhances J_{cp} , which may explain the experimental results of the wavenumber dependence of the integrated intensity of the neutron scattering. Additionally, a strong in-phase correlation between the nearest-neighbor corner-shared plaquette singlets increases because of the existence of J_{ed} due to the presence of the orbital order. Then the wavenumber of the lowest triplets may become $(0,0)$, which is consistent with the recent experimental results.¹³⁾ If this situation is true, small plaquette which is constructed by four oxygens without a V atom at the center may rotate or some other specific type of the lattice distortion may occur in order to favor the given orbital order. To obtain the information on the weight of these orbitals, a detailed analysis of the lattice structure is needed, especially at very low temperatures. Quantitative and detailed theoretical analyses of this proposal remain for further studies.

The orbital order effect may also be observed in the temperature dependence of χ for CaV_2O_5 .¹⁴⁾ This material also shows the spin gap behavior. The spin gap and the peak temperature are about 464K and 400K, respectively. One possible mechanism of the spin gap formation may be due to the ladder structure. Since it is assumed that d electron is localized at the d_{xy} orbital, the spin exchange couplings J in the leg and J_{\perp} in the rung have almost the same values. Numerical analysis of χ for the AFH model on the ladder lattice has led to the result that the ratio Δ_s/T_p is almost 0.5 at $J = J_{\perp}$.¹⁵⁾ However, the ratio obtained in the experiments is 1.16, which is different from the theoretical prediction. If the localized orbital on V atom is represented by the linear combination of the d_{xy} and one of the other t_{2g} orbitals which extends to the oxygen on the rung due to the orbital order, J_{\perp} becomes larger than J . Since the ratio Δ_s/T_p is 1.60 in the dimer limit ($J = 0$), it may become 1.16 as J increases from zero. Quantum or thermal fluctuation of the orbital degree of freedom also changes a quantitative behavior of χ at finite temperature. We propose that the orbital order of d_{xz} and d_{yz} orbitals with partially fillings of t_{2g} orbitals is also a promising explanation for rather puzzling experimental results in CaV_2O_5 . The quantitative study for this problem remains for further study.

§5. Summary

We have investigated orbital order effects in magnetic properties of CaV_4O_9 . Several possible models with the orbital order have been considered. The amplitudes of the spin exchange couplings for each model are determined in order to reproduce the temperature dependence of χ in experiments. The origins of the spin gap are not necessarily the same as the originally proposed plaquette

singlet but are ascribed to the generalized four-site singlet. By using the estimated values of the spin exchange couplings, the dispersion of the triplet excitations and the spin-spin correlation corresponding to the integrated scattering intensity have been calculated within the PE. The strong in-phase correlation between the nearest-neighbor pair of four-site singlets and the large antiferromagnetic spin correlation between the next nearest-neighbor spins are minimal requirements for the explanations of the experimental results in the neutron scattering. Although the wavenumber dependences of the triplet dispersion and the spin-spin correlation for our models do not show completely satisfactory agreement with those obtained by the presently available experimental data, they are much improved from the single-orbital cases. We further propose the mechanism required to explain each feature of the experimental results. We suggest that the order of the d_{xz} and d_{yz} orbitals hybridized with uniform and partial occupation of d_{xy} orbital may explain the experimental results. We have also discussed that effects of the orbital order may be observed in other vanadium oxide compounds such as CaV_2O_5 . These strongly suggest that the role of the orbital order is important in understanding the magnetic properties of the vanadium oxide compounds with the spin gap.

Acknowledgements

We would like to thank M. Sato, S. Taniguchi, K. Kodama for useful discussions and comments. We have used a part of the codes provided by H. Nishimori in TITPACK Ver.2. A part of the computation has been performed on VPP500 at the Supercomputer Center of the Institute for Solid State Physics, Univ. of Tokyo. This work is financially supported by a Grant-in-Aid for Scientific Research in Priority Areas “Anomalous Metallic States near the Mott Transition”.

Appendix A: Triplet Dispersion and Wavefunction by Perturbation Expansion

We introduce the procedure for calculating the energy dispersion of the lowest triplet band and the wavefunctions of the singlet ground state and the triplet band.

We first consider the model shown in Fig.4(a). The unperturbed Hamiltonian has the terms with J_{ep} on the edge-shared plaquette, while the other terms are treated as the perturbed ones. The ground state of the edge-shared plaquette with only J_{ep} is the RVB state $|\phi_{\text{g}}\rangle$. The energy of this state is $-2J_{\text{ep}}$. Then the ground state of the unperturbed Hamiltonian is the product state of $|\phi_{\text{g}}\rangle$ written as

$$|\Phi_{\text{g}}\rangle_{(a)} = \prod_i |\phi_{\text{g}}(\mathbf{r}_i)\rangle. \quad (\text{A}\cdot 1)$$

The lowest triplet states of the edge-shared plaquette $|\psi\rangle$ with $S_z = -1, 0, 1$ are the hopping state of the triplet pair in the RVB state. The energy of these states is $-J_{\text{ep}}$. Then the wavefunctions of the lowest triplet band are constructed by $|\psi\rangle$ on one of the edge-shared plaquette and $|\phi_{\text{g}}\rangle$ on the others. The degeneracy is lifted by the first-order perturbation. The wavefunctions of these

triplet states are written as

$$|\Psi(\mathbf{k})\rangle_{(a)} = \frac{1}{\sqrt{N_p}} \sum_i |\psi(\mathbf{r}_i)\rangle \prod_{j \neq i} |\phi_g(\mathbf{r}_j)\rangle e^{i\mathbf{k} \cdot \mathbf{r}_i}, \quad (\text{A.2})$$

where N_p is the number of the edge-shared plaquette. Within the second-order PE, the energy difference between the triplet states and the singlet ground state is represented as

$$\begin{aligned} \Delta_s(\mathbf{k})_{(a)} = & J_{\text{ep}} - \frac{115}{864} \frac{J^2}{J_{\text{ep}}} - \left(\frac{J}{3} + \frac{J^2}{72J_{\text{ep}}} \right) (\cos k_x + \cos k_y) \\ & + \frac{J^2}{108J_{\text{ep}}} (\cos 2k_x + \cos 2k_y) - \frac{J^2}{9J_{\text{ep}}} \cos k_x \cos k_y. \end{aligned}$$

Next, we consider the model shown in Fig.4(b). The unperturbed Hamiltonian has the terms with J_{ep} and J_{cd} on the edge-shared plaquette while the other terms are the perturbed ones. Since we take $J_{\text{cd}} > J_{\text{ep}}$, for example, $J_{\text{ep}} = 0.9J_{\text{cd}}$, the ground state of the edge-shared plaquette is not the $|\phi_g\rangle$ but the product state $|\xi_g\rangle$ of the dimer pair on each J_{cd} bond. The energy of this state is $-1.5J_{\text{cd}}$. Then the ground state of the unperturbed Hamiltonian is the product state of $|\xi_g\rangle$ written as

$$|\Phi_g\rangle_{(b)} = \prod_i |\xi_g(\mathbf{r}_i)\rangle. \quad (\text{A.3})$$

The wavefunctions of the lowest triplet states on the edge-shared plaquette are constructed by two states $|\eta\rangle$ and $|\zeta\rangle$ with $S_z = -1, 0, 1$ which are the product states of the triplet pair on one of the J_{cd} bond and the dimer pair on the others. Then the wavefunction of the lowest triplet bands are constructed from one of the triplets $|\eta\rangle$ or $|\zeta\rangle$ on one of the edge-shared plaquette and $|\xi_g\rangle$ on the others. The first-order perturbation lifts the degeneracy. The bonding and anti-bonding states of the triplets appear, which are written as

$$|\Psi_{\pm}(\mathbf{k})\rangle_{(b)} = \frac{1}{\sqrt{N_p}} \sum_{\mathbf{k}} \left(\frac{1}{\sqrt{10 \mp 4\sqrt{5}}} |\eta(\mathbf{r}_i)\rangle + \frac{-2 \pm \sqrt{5}}{\sqrt{10 \mp 4\sqrt{5}}} |\zeta(\mathbf{r}_i)\rangle \right) \prod_{j \neq i} |\xi_g(\mathbf{r}_j)\rangle e^{i\mathbf{k} \cdot \mathbf{r}_i}, \quad (\text{A.4})$$

in the parameter regions $0 \leq k_x \leq k_y \leq \pi$. Here J_{cp} and J_{ed} are both taken as J . The energy difference between these triplet states and the ground state is obtained as

$$\begin{aligned} \Delta_s(\mathbf{k})_{\pm} = & J_{\text{cd}} + \frac{3J^2}{8J_{\text{cd}}} - \frac{J^2}{16(J_{\text{cd}} - J_{\text{ep}})} - \frac{3J^2}{8(2J_{\text{cd}} - J_{\text{ep}})} - \frac{5J^2}{8(2J_{\text{cd}} + J_{\text{ep}})} \\ & + \left(\frac{J}{4} + \frac{J^2}{8J_{\text{cd}}} \right) \left[(-1 \mp \sqrt{5}) \cos k_x + (-1 \pm \sqrt{5}) \cos k_y \right]. \end{aligned}$$

In this model, the lowest singlet band is also calculated. In a similar way, the energy difference between the lowest singlet band and the singlet ground state is obtained as

$$\Delta'_s(\mathbf{k}) = 2(J_{\text{cd}} - J_{\text{ep}}) + \frac{9J^2}{8J_{\text{cd}}} - \frac{3J^2}{8J_{\text{ep}}} - \frac{J^2}{2(J_{\text{cd}} + J_{\text{ep}})} + \frac{J^2}{8J_{\text{ep}}} (\cos k_x + \cos k_y). \quad (\text{A.5})$$

Next we introduce the wavefunctions for the models shown in Fig.4(c). In the case shown in Fig.4(c), the unperturbed Hamiltonians are taken as the part with the relevant next-nearest-neighbor spin exchange couplings, while the other part with the relevant nearest-neighbor ones are the perturbed ones because we suggest that another possible origin of the spin gap is described as the stripe singlet in this case. Since the magnetic unit cell has two stripes, the ground state of the unperturbed Hamiltonians $|\Phi_g\rangle_{(c)}$ is represented by the product state of the stripe singlet $|\phi'_g(\mathbf{r}_i)\rangle_{1,2}$ on each stripe written as

$$|\Phi_g\rangle_{(c)} = \prod_i |\phi'_g(\mathbf{r}_i)\rangle_1 |\phi'_g(\mathbf{r}_i)\rangle_2, \quad (\text{A}\cdot6)$$

where the indices 1 and 2 represent the one stripe and the other stripe in the magnetic unit cell, respectively. The lowest triplet states of the magnetic unit cell for the unperturbed Hamiltonian are six-fold degenerated i.e. $|\psi'\rangle_1 |\phi'_g\rangle_2$ and $|\phi'_g\rangle_1 |\psi'\rangle_2$ with $S_z = -1, 0, 1$. Then the bonding and anti-bonding triplet bands appear by the PE. Within the first-order perturbation, the wavefunctions are obtained as

$$|\Psi_{\pm}(\mathbf{k})\rangle_{(c)} = \frac{1}{\sqrt{2N_s}} \sum_i (|\psi'(\mathbf{r}_i)\rangle_1 |\phi'_g(\mathbf{r}_i)\rangle_2 \pm |\phi'_g(\mathbf{r}_i)\rangle_1 |\psi'(\mathbf{r}_i)\rangle_2) \prod_{j \neq i} |\phi'_g(\mathbf{r}_j)\rangle_1 |\phi'_g(\mathbf{r}_j)\rangle_2, e^{i\mathbf{k} \cdot \mathbf{r}_i}, \quad (\text{A}\cdot7)$$

where N_s is the number of the stripe. We calculate the energy difference between these triplet bands and the ground state within the second-order PE written as

$$\Delta_s(\mathbf{k})_{\pm} = J'[A_1 \pm A_2(-\cos k_x + \cos k_y)], \quad (\text{A}\cdot8)$$

where the parameters A_1 and A_2 are 0.601 and 0.031, respectively at $J/J' = 0.38$. Here the component k_x and k_y are represented by the vectors $\tilde{\mathbf{a}}_1$ and $\tilde{\mathbf{b}}_1$, respectively.

Appendix B: Ground State Energy for Model in Fig. 4(c)

We calculate the ground state energy per site by the second-order PE to investigate the possible mechanism of the spin gap formation for the model shown in Fig.4(c). The first case is that the unperturbed Hamiltonian is the term with J_{ep} and the other terms are the perturbed Hamiltonian. In this case, the origin of the spin gap for the unperturbed Hamiltonian is the edge-shared plaquette singlet. The strength of the other spin exchange couplings is taken as J . The ground state energy per site is obtained as

$$\epsilon_g = -\frac{1}{2}J_{\text{ep}} + \frac{1}{16}J - \frac{11}{576}\frac{J^2}{J_{\text{ep}}}. \quad (\text{B}\cdot1)$$

The second case is that the unperturbed Hamiltonian is the term with J_{ed} while the others are the perturbed ones. The strength of the other spin exchange couplings is taken as J . In this case, the origin of the spin gap is the dimer singlet. The ground state energy per site is obtained as

$$\epsilon_g = -\frac{3}{8}J_{\text{ed}} - \frac{9}{128}\frac{J^2}{J_{\text{ed}}}. \quad (\text{B}\cdot2)$$

The third case is that the term with the next-nearest-neighbor spin exchange coupling J' is the unperturbed Hamiltonian while the others are the perturbed ones. Similarly, the strength of the other spin exchange coupling is taken as J . In this case, the origin of the spin gap is the stripe singlet. The ground state energy per site is obtained as

$$\epsilon_g = -\frac{3+2\sqrt{3}}{16}J' - \frac{J^2}{J'}\left(\frac{A}{8} + \frac{B}{4}\right), \quad (\text{B}\cdot 3)$$

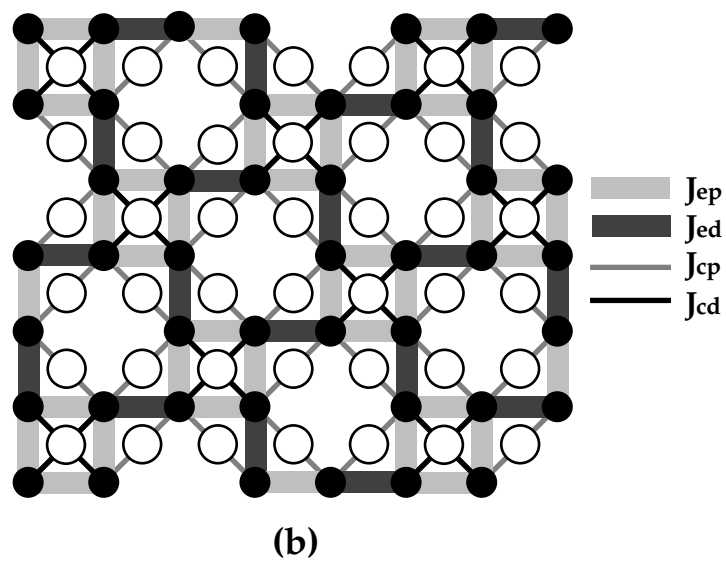
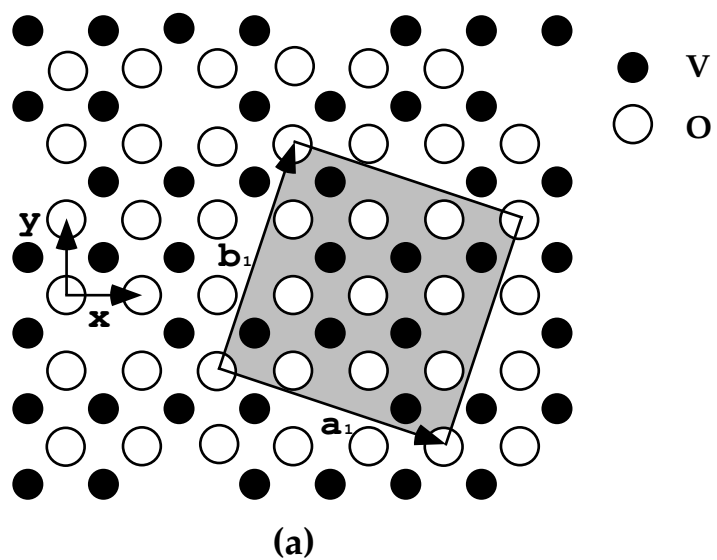
where the parameters A and B are written as

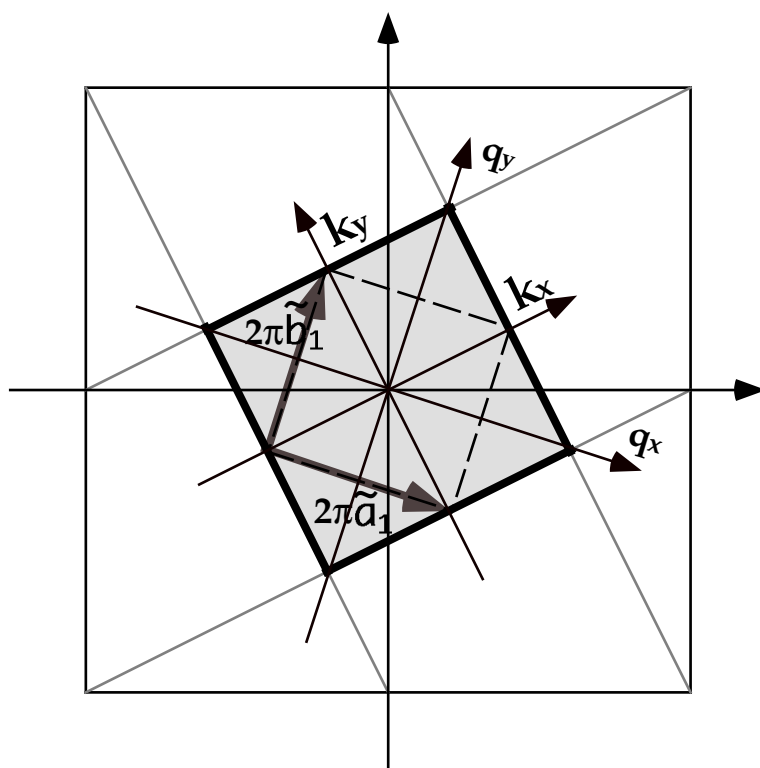
$$A = \frac{1}{3(1+\sqrt{3})}, \quad (\text{B}\cdot 4)$$

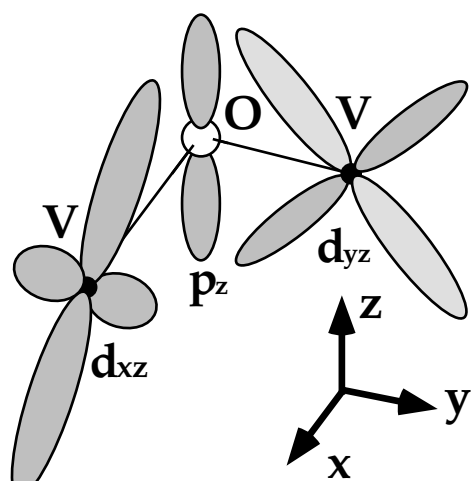
$$B = \frac{1}{768} \left[\frac{(4-\sqrt{2}-2\sqrt{3}+\sqrt{6})^2}{1-\sqrt{2}+\sqrt{3}} + \frac{(2-3\sqrt{2}+\sqrt{6})^2}{1+\sqrt{3}} + \frac{8(\sqrt{3}-1)^2(2-\sqrt{2})}{2-\sqrt{2}+2\sqrt{3}} \right. \\ \left. + \frac{(-4-\sqrt{2}+2\sqrt{3}+\sqrt{6})^2}{1+\sqrt{2}+\sqrt{3}} + \frac{(2+3\sqrt{2}+\sqrt{6})^2}{1+\sqrt{3}} + \frac{8(\sqrt{3}-1)^2(2+\sqrt{2})}{2+\sqrt{2}+2\sqrt{3}} \right],$$

respectively. When the parameters J_{ep} and J_{ed} are taken as J , the $J/(J+J')$ dependence of the ground state energy per site is obtained, as shown in Fig.7.

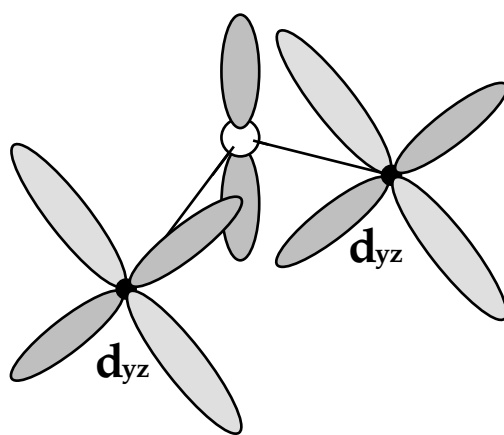
-
- [1] S. Taniguchi, T. Nishikawa, Y. Yasui, Y. Kobayashi, M. Sato, T. Nishioka, M. Kotani and K. Sano: J. Phys. Soc.Jpn. **64** (1995) 2758
 - [2] N. Katoh and M. Imada: J. Phys. Soc. Jpn. **64** (1995) 4105
 - [3] K. Ueda, H. Kontani, M. Sigrist and P. A .Lee: Phys. Rev. Lett. **76** (1996) 1932
 - [4] M. P. Gelfand, Z. Weihong, R. R. P. Singh, J. Oitmaa and C. J. Hamer: Phys. Rev. Lett. **77** (1996) 2794
 - [5] K. Sano and A. Takano: J. Phys. Soc. Jpn. **65** (1996) 1514
 - [6] K. Takano and K. Sano: preprint
 - [7] M. Albrecht and F. Mila: Phys. Rev. B **53** (1996) 2945
 - [8] O. A. Starykh, M. E. Zhitomirsky, D. I. Khomskii, R. R. P. Singh and K. Ueda: Phys. Rev. Lett. **77** (1996) 2558
 - [9] M. Troyer, H. Kontani and K. Ueda: Phys. Rev. Lett. **76** (1996) 3822
 - [10] S. R. White: Phys. Rev. Lett. **77** (1996) 3633
 - [11] T. Miyazaki and D. Yoshioka: J. Phys. Soc. Jpn. **65** (1996) 2370
 - [12] K. Kodama, H. Harashina, S. Shamoto, S. Taniguchi, M. Sato, K. Kakurai and M. Nishi: J. Phys. Soc. Jpn. **65** (1996) 1941
 - [13] K. Kodama, H. Harashina, H. Sasaki, Y. Kobayashi, M. Kasai, S. Taniguchi, Y. Yasui, M. Sato, K. Kakurai, T. Mori and M. Nishi: J. Phys.Soc. Jpn. **66** (1997) 793
 - [14] H. Iwase, M. Isobe, Y. Ueda and H. Yasuoka: J. Phys. Soc. Jpn. **65** (1996) 2397
 - [15] M. Troyer, H. Tsunetsugu and D. Würtz: Phys. Rev. B **50** (1994) 13515
 - [16] S. Marini and D. I. Khomskii: preprint



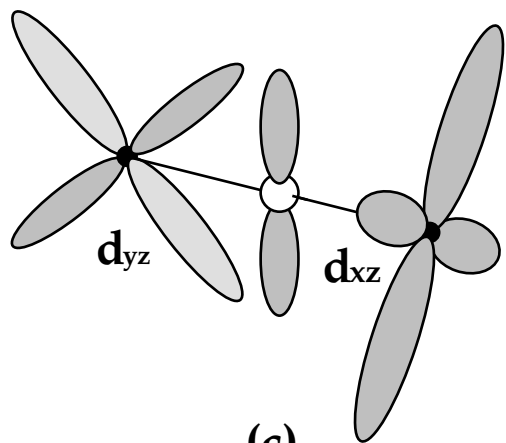




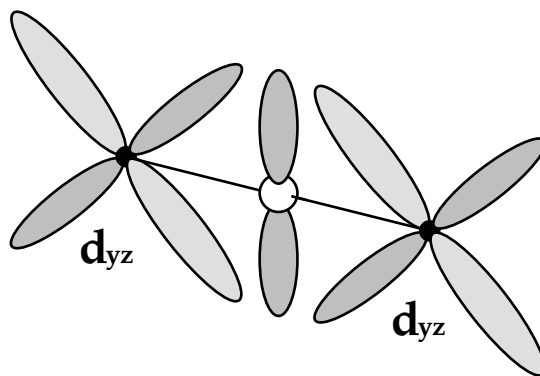
(a)



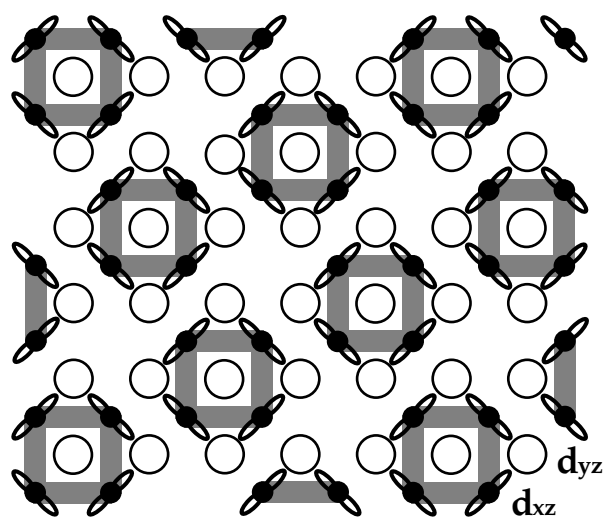
(b)



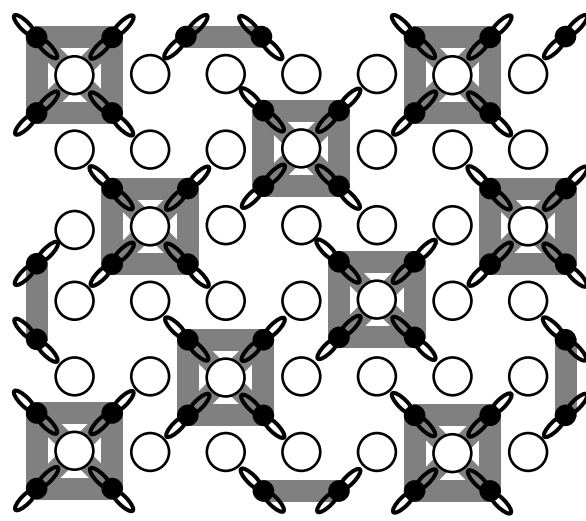
(c)



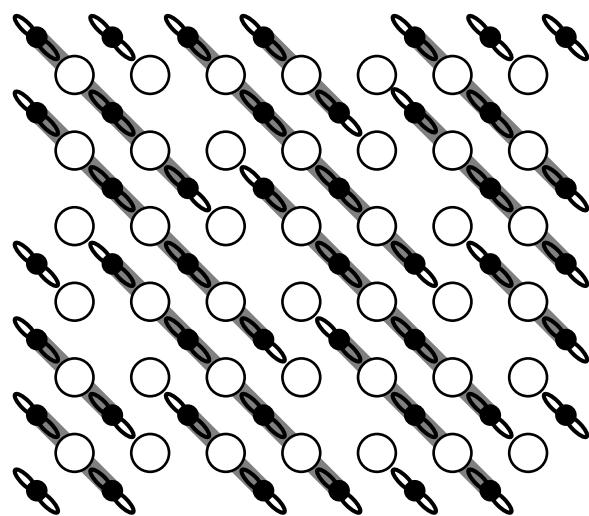
(d)



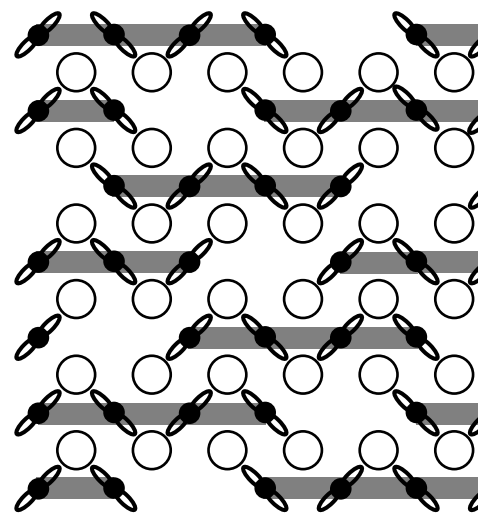
(a)



(b)



(d)



(e)

